




Coherent control of thermoelectric currents and noise in quantum thermocouples

José Balduque  and Rafael Sánchez 

Departamento de Física Teórica de la Materia Condensada, Condensed Matter Physics Center (IFIMAC), and Instituto Nicolás Cabrera, Universidad Autónoma de Madrid, 28049 Madrid, Spain

 (Received 27 July 2023; revised 17 November 2023; accepted 3 January 2024; published 23 January 2024)

Three-terminal coherent conductors are able to perform as quantum thermocouples when the heat absorbed from one terminal is transformed into useful power in the other two. Allowing for a phase coherent coupling to the heat source, we introduce a way to control and improve the thermoelectric response via quantum interference. A simple setup composed of a scanning probe between two resonant tunneling regions is proposed that achieves better performance than incoherent analogs by enhancing the generated power and efficiency and reducing the output current noise.

DOI: [10.1103/PhysRevB.109.045429](https://doi.org/10.1103/PhysRevB.109.045429)

I. INTRODUCTION

The importance of phase coherence in transport through mesoscopic electrical conductors is well-known [1,2]. When the system size is small with respect to the length at which carriers decohere in their propagation (i.e., the coherence length), the phases accumulated within the sample induce quantum interference effects that manifest in the mean currents through the system, see, e.g., Ref. [3] for a discussion of experimental realizations. The resulting sharp spectral features (e.g., Fabry-Pérot-like or Fano-like resonances and destructive Aharonov-Bohm interference) can be used as energy filters, one of the requirements to find thermoelectric devices able to efficiently convert heat into electrical power [4–9]. Recent experiments using quantum dots (QDs) have confirmed these expectations [10,11]. Phase coherence can then induce a thermoelectric response in conductors that would not manifest it in the absence of interference. Furthermore, this response can be controlled externally in different configurations including magnetic fields [12–15], gate voltages [16], and movable junctions [17]. Interferences have also been used to enhance the thermoelectric efficiency [18–21].

Multiterminal configurations [22,23] contain the nonlocal thermoelectric effect: a charge current is measured in an isothermal conductor formed by two terminals at the same temperature and electrochemical potential out of the conversion of heat injected from one or more other terminals. They introduce the possibility to inject heat directly into the mesoscopic region, allowing one to probe the energetics of internal processes, including electron-electron interactions [24–27], phonon- [28–33] and photon-assisted tunneling [34], fluctuating potentials [35–37], thermalization [11,38–41], local hotspots [17,42], and Kondo correlations [43] in semiconductor devices (with connections with models of hot carrier solar cells [44–47], nothing avoids the sun to be the third terminal of a mesoscopic conductor), Cooper-pair splitting [48–53], or Andreev reflection [54–56] in QDs proximitized with a superconductor, and chirality [57–59] and helicity [60,61], or nonthermal states [62] in quantum Hall edge channels. In

most of the above works, the phase coherence of the particles injected from the hot source is lost as they enter the conductor. However, coherently coupling to the hot terminal [42] makes the source responsible for the thermoelectric response not only for providing heat but also for inducing the necessary energy filtering via quantum interference. Unfortunately, though this effect enhances the longitudinal thermoelectric response substantially [42], the nonlocal thermoelectric efficiency remains tiny [17].

This effect evidences that the coupling to the heat source can dramatically change the conduction properties of a system. Think, for instance, of using the resulting interference to enhance transport between some pairs of terminals while suppressing it into some others. We are interested in finding the simplest configurations where such effect leads to efficient heat to power conversion. For this, we consider a one-dimensional two-terminal conductor with two regions where electrons are scattered (defined by scattering matrices S_α , with $\alpha = 1, 2$). The two regions are separated by a distance d short with respect to the electron mean-free path (we assume ballistic propagation). This separation can be scanned by the tip of a

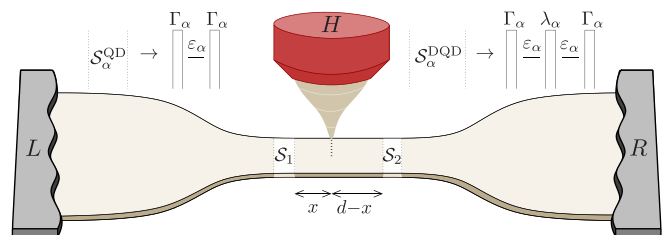


FIG. 1. Scheme of the quantum thermocouple. A quasi-one-dimensional quantum conductor connected to two isothermal terminals, L and R , is coupled to a third hot terminal, H , via the tip of a scanning probe. The tip scans the region between two scatterers, represented by the scattering matrices S_α , $\alpha = 1, 2$, and separated by a distance d . We chose these scatterers to be either resonant tunneling single or double quantum dots with couplings Γ_α and λ_α , and resonance energies ϵ_α , as indicated in the inset.

tunneling microscope [63–65] which exchanges particles with the conductor (though we will assume that the injected particle current is zero in average). The tip couples the conductor to a third terminal, H , that acts as the heat source, see Fig. 1. Transport between every two terminals depends not only on the properties of the two scattering regions α but also on the internal reflections involving the tip. Therefore, the position of the tip, situated at a distance x from the scattering region 1, can be used to shape the transmission probabilities between all three terminals in a way that can be controlled experimentally. Using this property, the system thermoelectric response can be tuned. Nanometer-resolved nonlocal thermoelectric responses have been achieved in one- [66,67] and two-dimensional samples [68–70] via different kinds of scanning probes.

Here we will consider two cases depending on the chosen structure of the two conductor scattering regions: when they are given by single resonant tunneling QDs, demonstrated experimentally to be efficient energy harvesters [11], or by double quantum dots (DQDs). The performance will be quantified in terms of the generated electrical power, the thermoelectric efficiency, and the signal to noise ratio of the current output. Ideally, one aims for a conductor that is able to generate a large power output with low noise and high efficiency. In practice, one needs to find a compromise: typically, high efficiencies occur at the expense of low power outputs [9], for instance, in the case of very narrow resonances. A practical alternative is to try to improve the efficiency at a given power output that one needs to run a particular device. In that case, systems with boxcarlike transmission probabilities are found to be optimal in two terminal setups [7,71,72]. The problem has also been explored in three-terminal coherent conductors, finding similar boxcar transmissions between the conductor terminals and the heat source combined with the extra requirement of having no elastic transfer of particles between the conductor terminals, L and R [73]. This means that all electrons flowing along the device are forced to visit the heat source connected to the mesoscopic region in their way. Such broadband transmission probabilities are difficult to find without requiring complicated structures formed by multiple QDs [7,74,75]. Another possibility is to consider configurations with broken time-reversal symmetry, either by a magnetic field [39,76–79] or by ac driving [80,81]. A clear interest appears in finding simpler and easier to control configurations.

The current noise is also important in mesoscopic conductors [82,83]. From an operational point of view, trying to reduce the fluctuations adds a different point of view for optimization [84–90]. One can naively expect that boxcar transmissions are also beneficial for reducing the noise signal: the partition noise contribution in two-terminal devices will vanish as transmission is either 0 or 1. Fluctuations in three-terminal configurations are somewhat more complicated and need to be explored. Note, however, that, apart from this practical issue, the fluctuations contain fundamental information about the quantum heat engine dynamics [91–94].

We will compare the fully coherent configuration with existing (inelastic) energy harvesters in which carriers are fully thermalized at the heat source [11,40]. They consist of a hot central reservoir directly coupled to the two conductor terminals via (single) resonant tunneling QDs (as in the QD

case) achieving efficient energy harvesting. We will refer to them as QD-th in the following. Our results show that resonant filtering combined with internal reflections lead to boxcar-shaped transmissions that improve the power, efficiency, and signal-to-noise ratio as compared to incoherent case.

The remainder of the paper is organized in the following way. In Sec. II, we introduce the theoretical description of transport (currents and noises) based on noninteracting scattering theory, as well as the performance quantifiers, and show the resulting zero bias transport properties in Sec. III. In Sec. IV, we discuss the optimization procedure and the results obtained for the different configurations. Conclusions are presented in Sec. V.

II. SCATTERING APPROACH

A. Transport and noise formulas

We are interested in the simplest description of transport through multiterminal quantum coherent conductors where correlations due to electron-electron interactions can be disregarded (for related configurations including electron-electron interactions, see, e.g., Refs. [95,96]). This regime is well described by the Landauer-Büttiker scattering theory [1,97]. Assuming that the system has a single channel, the transport properties between terminals l and l' are encoded in the scattering matrix $\mathcal{S}_{l'l}$. With it, we can calculate the mean particle and heat currents [98,99] flowing out of terminal $l = L, R, H$:

$$I_l = \frac{2}{h} \sum_{l'} \int dE \mathcal{T}_{l'l}(E) [f_l(E) - f_{l'}(E)], \quad (1)$$

$$J_l = \frac{2}{h} \sum_{l'} \int dE (E - \mu_l) \mathcal{T}_{l'l}(E) [f_l(E) - f_{l'}(E)], \quad (2)$$

where $\mathcal{T}_{l'l}(E) = |\mathcal{S}_{l'l}(E)|^2$ is the transmission probability from l to l' and $f_l(E) = \{1 + \exp[(E - \mu_l)/k_B T_l]\}^{-1}$, the Fermi distribution function of terminal l having an electrochemical potential μ_l , and a temperature T_l ; the factor 2 accounts for spin degeneracy in the absence of a magnetic field, in which case we also have that $\mathcal{T}_{l'l}(E) = \mathcal{T}_{l'l'}(E)$. For the charge current, one multiplies Eq. (1) by $-e$. Note that the thermoelectric effect requires that the transmission probabilities depend on energy: if all terminals are grounded, $\mu_l = \mu$, $\forall l$, no filtering leads to $I_l = 0$, as $\int dE [f_l(E) - f_{l'}(E)] = 0$. We emphasize that all heat currents are carried by electrons: at low (tens of mK) temperatures, the electron-phonon coupling can be neglected.

We can also calculate the current-current correlations $S_{X_l X_{l'}}(t - t') = \langle \{\Delta \hat{X}_l(t), \Delta \hat{X}_{l'}(t')\} \rangle / 2$, with $\Delta \hat{X}_l(t) \equiv \hat{X}_l(t) - X_l$, where the mean current $X_l = I_l$, J_l is the statistical average of the current operator: $X_l = \langle \hat{X}_l(t) \rangle$ [100]. Following Ref. [82], one obtains the zero frequency noise (autocorrelations), which can be decomposed in thermal (th) and shot (sh) noise contributions, $S_{l,l} = S_{l,l}^{\text{th}} + S_{l,l}^{\text{sh}}$. For a three-terminal configuration ($l, l', m = L, R, H$), they read

$$S_{l,l}^{\text{th}} = \frac{4}{h} \int dE \sum_{l' \neq l} \mathcal{T}_{l'l'} [f_l(1 - f_l) + f_{l'}(1 - f_{l'})] \quad (3)$$

and

$$S_{I_H}^{\text{sh}} = \frac{4}{h} \int dE \left[\sum_{l', m \neq l} \frac{\mathcal{T}_{l'l} \mathcal{T}_{lm}}{2} (f_{l'} - f_m)^2 + \sum_{l'} \mathcal{T}_{ll'} \mathcal{T}_{l'l} (f_{l'} - f_l)^2 \right]. \quad (4)$$

For the heat noise, $S_{J_l J_l}$ [101,102], one needs to include $(E - \mu_l)^2$ in the integrals of the above Eqs. (3) and (4). The expression for heat-charge crosscorrelations (aka mixed noise) is slightly more cumbersome:

$$S_{I_l J_{l'}} = \frac{4}{h} \int dE (E - \mu_{l'}) \left\{ \sum_r \mathcal{T}_{lr} \mathcal{T}_{l'r} f_r (1 - f_r) - \mathcal{T}_{ll'} [f_l (1 - f_l) + f_{l'} (1 - f_{l'})] + \frac{1}{4} \sum_{r \neq r'} \mathcal{M}_{ll', rr'} [f_r (1 - f_{r'}) + f_{r'} (1 - f_r)] \right\}, \quad (5)$$

where we have defined

$$\mathcal{M}_{ll', rr'} \equiv \mathcal{S}_{lr}^\dagger \mathcal{S}_{l'r'} \mathcal{S}_{l'r}^\dagger \mathcal{S}_{l'l'} + \mathcal{S}_{lr} \mathcal{S}_{l'r'}^\dagger \mathcal{S}_{l'r} \mathcal{S}_{l'l'}^\dagger. \quad (6)$$

In the following, we will concentrate on correlations including the heat current injected from the tip and the generated current in terminal R . Hence, we will simplify the notation as $S_{II} \equiv S_{I_R I_R}$, $S_{JJ} \equiv S_{J_H J_H}$, and $S_{IJ} \equiv S_{I_R J_H}$.

B. Scattering components

We will focus on a three-terminal conductor working as an energy harvester as the one depicted in Fig. 1. A one-dimensional elastic conductor composed of two terminals, $l = L, R$, at the same temperature, T , and with electrochemical potential μ_l are connected by two scattering regions $\alpha = 1, 2$ with scattering matrices

$$\mathcal{S}_\alpha = \begin{pmatrix} r_\alpha & \tau_\alpha \\ \tau_\alpha & r_\alpha \end{pmatrix}, \quad (7)$$

where r_α and τ_α are the reflection and transmission amplitudes, respectively, and fulfill $|r_\alpha|^2 + |\tau_\alpha|^2 = 1$. We consider single-channel junctions, for simplicity. We will investigate two different configurations (sketched in Fig. 1) where the two scattering regions are either a resonant tunneling QD, with Breit-Wigner amplitudes [103],

$$\tau_\alpha^{\text{QD}}(E) = \frac{-i\Gamma_\alpha}{E - \varepsilon_\alpha + i\Gamma_\alpha}, \quad (8)$$

$$r_\alpha^{\text{QD}}(E) = 1 + \tau_\alpha^{\text{QD}}(E),$$

with resonance energy ε_α and broadening Γ_α , or a double QD [104] (see Appendix for details),

$$\tau_\alpha^{\text{DQD}}(E) = -\frac{i\Gamma_\alpha \lambda_\alpha}{(E - \varepsilon_\alpha + i\Gamma_\alpha/2)^2 - \lambda_\alpha^2}, \quad (9)$$

$$r_\alpha^{\text{DQD}}(E) = 1 + \frac{(E - \varepsilon_\alpha + i\Gamma_\alpha/2)}{\lambda_\alpha} \tau_\alpha^{\text{DQD}}(E),$$

where λ_α is the interdot coupling. We assume symmetric DQDs, each one described by a single resonance energy, ε_α ,

and coupling Γ_α , for simplicity. We will later also consider that $\Gamma_1 = \Gamma_2 = \Gamma$ (both in the QD and DQD cases) and $\lambda_1 = \lambda_2 = \lambda$. Noninteracting DQDs have recently been used to indicate deviations of the fluctuations in coherent transport from classically established thermodynamic bounds [105,106].

The two regions are separated by a distance d . A third terminal, H , at temperature $T_H = T + \Delta T$ and electrochemical potential μ_H is coupled to the conductor via the tip of a scanning tunneling probe at a distance $x < d$ of the scattering region 1. Scattering at the conductor-tip junction is given by the matrix [63,107]

$$\mathcal{S}_{\text{tip}} = \begin{pmatrix} -\eta_-/2 & \sqrt{\epsilon} & \eta_+/2 \\ \sqrt{\epsilon} & \eta_- - 1 & \sqrt{\epsilon} \\ \eta_+/2 & \sqrt{\epsilon} & -\eta_-/2 \end{pmatrix}, \quad (10)$$

where $\eta_\pm = 1 \pm \sqrt{1 - 2\epsilon}$. The real parameter $\epsilon \in [0, 1/2]$ quantifies the tip-conductor coupling. The tip-conductor geometry permits to uncouple the heat source when $\epsilon = 0$, in which case the system behaves as an isothermal two-terminal conductor.

The hot terminal is assumed to be a voltage probe [108] with a floating electrochemical potential which will adapt to the condition $I_H = 0$. This way, heat but no net charge is injected through the tip into the conductor. Note that the heat injection mechanism is fully coherent and adds to the interferences due to internal reflection in the conductor. Electrons propagating within scattering regions with wave number $k(E) = \sqrt{2m(E - U_0)}/\hbar$ will accumulate a kinetic phase $\chi_x(E)/2 = k(E)x$ in their way between 1 and the tip, and $\chi_{d-x}(E)/2 = k(E)(d - x)$ between the tip and 2. We take the energy of the lowest subband of the one-dimensional conductor [3] as the energy origin, $U_0 = 0$. In the ballistic regime, we can safely neglect disorder effects in the nanowire potential [109]. The region between \mathcal{S}_1 and \mathcal{S}_2 can be viewed as a double Fabry-Pérot interferometer with a movable intermediate barrier which has the particularity that it absorbs and reinjects particles. The energy dependence of the accumulated phases are sufficient to induce a thermoelectric effect in interferometers [12–17] or to enhance it [18,20,21].

C. Shaping the transmission probabilities

Known the scattering matrices of the two scattering regions and the tip junction, Eqs. (7) and (10), as well as the phases accumulated in the connections between them, χ_{d-x} and χ_x , we are ready to obtain the scattering matrix of the whole system. For this, one simply needs to take into account that, e.g., the right-outgoing wave from region 1 is the left-ingoing wave at the tip, multiplied by a phase factor $e^{i\chi_x(E)/2}$, and the same for the wave going out of the tip and scattering at 2 with a factor $e^{i\chi_{d-x}(E)/2}$ instead, and solve for all the outgoing waves as functions of the ingoing ones, see, e.g., Ref. [1] or Ref. [17] for a more related configuration.

The resulting scattering matrix $S(E)$ connects the three terminals L , R , and H . The obtained transmission probabilities can be decomposed as

$$\mathcal{T}_{IH}(E) = 2\epsilon |\mathcal{A}|^{-2} |\tau_{\alpha_l}|^2 \mathcal{I}_{IH}, \quad (11)$$

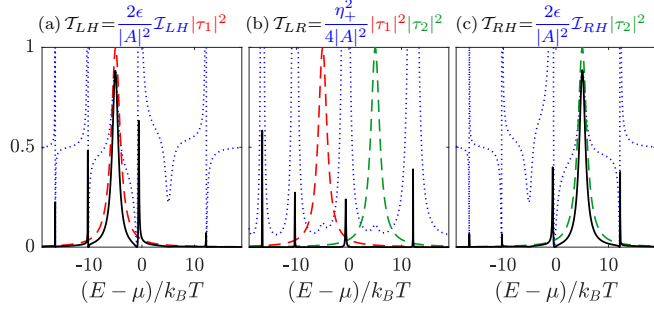


FIG. 2. Transmission probabilities between (a) terminals L and H , (b) terminals L and R , and (c) terminals R and H as a function of the energy of the scattered electrons when scattering regions 1 and 2 correspond to the single QD case. The total transmission (black full line) can be decomposed as suggested in Eqs. (11) and (12) (red/green dashed: transmission probability of quantum dots 1,2; blue dotted: contribution from the multiple internally reflected trajectories between scattering regions and the tip). Parameters: $d = 10l_0$, $x = d/2$, $\epsilon = 0.5$, $\Delta E = 10k_B T$, $\Gamma = k_B T$, $\mu = 20k_B T$.

for trajectories between terminals $l = L, R$, and H , with $\alpha_{L(R)} = 1(2)$, and

$$\mathcal{T}_{LR}(E) = \frac{\eta_+^2}{4|A|^2} |\tau_1|^2 |\tau_2|^2, \quad (12)$$

for elastic transport along the conductor (without visiting the probe terminal). In these expressions, τ_α are the transmission amplitudes at scatterer α , see Eqs. (8) and (9), while

$$A = 1 + \frac{\eta_-}{2} (r_1 e^{i\chi_x} + r_2 e^{i\chi_{d-x}}) - \sqrt{1-2\epsilon} r_1 r_2 e^{i\chi_d}, \quad (13)$$

where $\chi_d = \chi_x + \chi_{d-x}$, and

$$\mathcal{I}_{lH}(E) = 1 - \frac{|\tau_{\beta_l}|^2}{2} + \text{Re}[r_{\beta_l} e^{i\chi_l}] \quad (14)$$

account for the quantum interference of multiple internally reflected trajectories between the QDs and the tip, with $\chi_{L(R)} = \chi_{d-x}(\chi_x)$ and $\beta_{L(R)} = 2(1)$. As the scattering matrix is unitary, reflection probabilities can be calculated from the transmissions: $\mathcal{T}_{ll} = 1 - \sum_{l' \neq l} \mathcal{T}_{ll'}$.

As an illustration, the three transmissions are plotted in Fig. 2 for the case of QD scatterers when the tip is right in the middle distance between them. Henceforth, lengths are expressed in units of $l_0 = \hbar/\sqrt{8mk_B T}$, which for GaAs wires is of the order of 40 nm at $T = 1$ K. We will also assume that the tip is strongly coupled, $\epsilon \lesssim 0.5$, which gives the largest power [17]. While $|\tau_\alpha^{\text{QD}}|^2$ give Lorentzian line shapes around the energies ε_1 (red-dashed line) and ε_2 (green-dashed line), the interference patterns (blue-dotted lines) strongly influence the total transmission probabilities (full black lines), which show Fano-shaped narrower tunneling resonances at ε_α and additional very sharp peaks. To understand the Fano-like interference, one can think of the closed trajectories formed between the tip and the reflecting barrier (scatterer 2 for \mathcal{T}_{LH} , scatterer 1 for \mathcal{T}_{RH}) as playing the role of a localized state in parallel to trajectories that are transmitted through the other barrier and the tip. Of particular interest for our purposes here is the destructive interference that strongly suppresses the elastic contribution between L and R , see Fig. 2(b).

Note that the developed interference patterns require scatterers with broad spectral features. In this sense, the weak coupling limit where $\Gamma_\alpha \ll k_B T$, so $|\tau_\alpha^{\text{QD}}|^2 \approx \Gamma_\alpha \delta(E - \varepsilon_\alpha)$, is not particularly useful.

D. Thermoelectric response

Transport between the two conductor terminals, L and R , consists of two contributions. On top of the elastic transmission between L and R , $\mathcal{T}_{LR}(E)$, sequential transmission between the conductor terminals and the tip, given by $\mathcal{T}_{LH}(E)$ and $\mathcal{T}_{HR}(E)$, introduces an inelastic contribution. The current can be decomposed in the two contributions, $I_R = I_{\text{el}} + I_{\text{inel}}$, with

$$I_{\text{el}} = \frac{2}{h} \int dE \mathcal{T}_{LR}(E) [f_R(E) - f_L(E)], \quad (15)$$

$$I_{\text{inel}} = \frac{2}{h} \int dE \mathcal{T}_{HR}(E) [f_R(E) - f_H(E)], \quad (16)$$

with particle conservation $I_L = -I_R$ being guaranteed by the probe condition, $I_H = 0$. In the absence of an applied voltage, the elastic contribution vanishes (remember $T_L = T_R$). Even worse, as a finite bias is applied, the elastic contribution will always flow downhill, i.e., dissipating (Joule) power. Hence, the thermoelectric power generation relies on the inelastic contribution [8,110]. Note that the inelastic scattering contribution is not describing heat leakage with an environmental bath but rather with an electronic reservoir that is treated in equal footing as the conductor terminals.

At zero bias, a finite current will flow as soon as the energy dependence of $\mathcal{T}_{LH}(E)$ and $\mathcal{T}_{HR}(E)$ are different. The sign of the current will be determined by the dominance of hole- or electronlike character of the two lead-tip transmissions, similar from what one expects in a conventional thermocouple [9]. In our case, this can be controlled with the energy gain $\Delta E \equiv \varepsilon_2 - \varepsilon_1$ given by the position of the resonances (measured with respect to the equilibrium electrochemical potential, μ), and tuned by gate voltages. It is also modulated with the internal interferences depending on the position of the tip, x .

Then, a finite power, $P = -I_R \Delta\mu > 0$, will be generated as long as the inelastic contribution flowing against the electrochemical potential difference $\Delta\mu \equiv \mu_R - \mu_L$ (applied symmetrically around μ) is larger than the elastic one flowing in favor. The maximal generated power in a quantum channel connecting two electronic reservoirs with different temperatures turns out to be limited by quantum mechanical effects [111], as found in Refs. [7,112], with the bound given by

$$P_W = 2A_0 \frac{\pi^2}{h} k_B^2 \Delta T^2, \quad (17)$$

where $A_0 \simeq 0.0321$, the factor 2 accounts for spin degeneracy, and ΔT is the temperature difference between reservoirs. This is a two-terminal result, so to compare with an optimal thermocouple heat engine that consists of two systems with opposite thermoelectric responses, we have to multiply by a factor 2.

Another way to quantify the thermoelectric performance is the efficiency, $\eta = P/J_H$, whose thermodynamic bound is, not very surprisingly [73], established by the Carnot efficiency,

$\eta_C = 1 - T/T_H$. However, it is not the main limitation in this case, as quantum mechanical effects establish a stronger bound for the efficiency at any given power output, η_W [7]. Although there is not analytical expression for this value, it is possible to obtain it numerically following Ref. [112] by finding the narrower boxcar transmission that results in the chosen power, which also depends on the choice of applied bias. One usually needs to find a compromise between high power output and high efficiency, which may depend on the desired operation at task.

Additionally, one wants that the generated power does not strongly fluctuate. This question has generated strong interest in the last years related to thermodynamic bounds on the amount of fluctuations depending on the entropy produced by the engine. These are the so-called thermodynamic uncertainty relations, initially obtained for classical stochastic engines [113] and shown to be modified in the presence of quantum coherence [105,114,115] and generalized for multi-terminal configurations [56,116]. Here we will adopt a more practical strategy and quantify the signal-to-noise ratio via the particle current inverse Fano factor [82]:

$$\frac{1}{F} = \frac{2|I_R|}{S_{I_R}}. \quad (18)$$

Note that while the isothermal transport of noninteracting electrons is sub-Poissonian ($F < 1$) [82], there is no such restriction in the presence of a temperature difference: think, for instance, of the stopping voltage where current vanishes on average but fluctuations do not, see, e.g., Ref. [88]. We will not compare with any complicated bound; here we are simply interested in trying to keep $1/F$ as high as possible.

E. Thermalized cavity model

To emphasize the quantum coherent effects, we will compare the performance of the above models with an energy harvester where the two scatterers (formed by single resonant tunneling QDs) couple the two conductor terminals directly to the hot reservoir. This way, electrons are thermalized in H as they tunnel from the conductor terminals through the QDs. Hence, the elastic contribution vanishes, as $\mathcal{T}_{LR}^{\text{QD-th}}(E) = 0$, and currents are fully determined by the transmission probabilities $\mathcal{T}_{iH}^{\text{QD-th}}(E) = \Gamma_{\alpha_i}^2 / [(E - \varepsilon_{\alpha_i})^2 + \Gamma_{\alpha_i}^2]$ which enter the inelastic transport [40]. Note this model cannot be obtained from the limit of a strongly coupled tip ($\epsilon \rightarrow 1/2$) in the QD setup: terminal H requires two channels to avoid interference [117].

III. ZERO BIAS TRANSPORT

Let us first consider the transport properties of the unbiased conductor with $\mu_L = \mu_R = \mu$. Without coupling to the hot reservoir ($\epsilon = 0$), all currents are zero, as expected for a system in equilibrium. Only noise will be finite due to the thermal fluctuations, see Eq. (3). As the tip is coupled, electrons in the conductor at a distribution $f_L(E) = f_R(E)$ can be absorbed by terminal H and be reinjected with a hotter distribution $f_H(E)$, leading to a heat current J_H . This process breaks detailed balance provided $\mathcal{T}_{LH}(E) \neq \mathcal{T}_{RH}(E)$: Consider, for instance, the configuration shown in Fig. 2, where $\mathcal{T}_{LH}(E)$ is, on average,

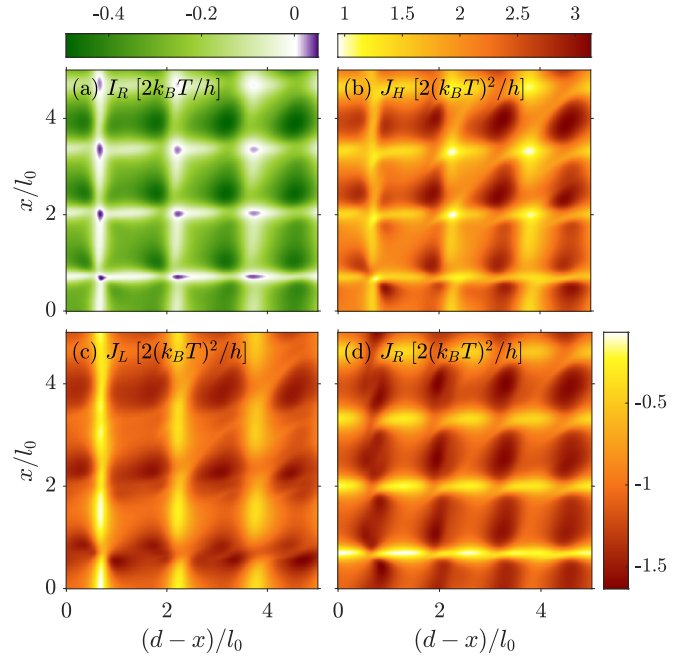


FIG. 3. (a) Generated thermoelectric current, I_R , and (b)–(d) heat currents in reservoirs $l = H, L, R, J_l$, when the temperature of reservoir H is increased by $\Delta T/T = 1$ and the scatterers are single quantum dots, with $\Delta\mu = 0$. Parameters: $\Delta E = 6k_B T$, $\epsilon = 0.5$, $\Gamma = 2k_B T$, $\mu = 20k_B T$.

more weighted for energies below the electrochemical potential, with the opposite being true for $\mathcal{T}_{RH}(E)$, for instance, if $\Delta E > 0$. Then, cold electrons from L will most likely be absorbed by the tip than those from R ; similarly, the reinjected hot electrons will most likely be transferred to R than to L . As a result, a net current will flow from L to R . The position of the tip modulates the energy dependence transmission probabilities $\mathcal{T}_{iH}(E)$, resulting in periodic oscillations which suppress the generated current. Eventually, the current changes sign for low ΔE . This is shown in Fig. 3(a) as a function of the distances from the tip to the two scatterers. This is an effect of interference not present in the QD-th configuration with similar QDs [40]. Similar oscillations show up in the heat currents [17] flowing out of the hot terminal and into the conductor ones, with the maxima of all four currents occurring in the same regions, see Figs. 3(b)–3(d). Note that in some regions all currents are suppressed, suggesting that the tip works as a valve. Note also that the heat currents are suppressed in the symmetric condition $x = d/2$, with replicated features parallel to this condition. Remarkably, the spots where I changes sign coincide with the minima of the injected J_H , which may be attributed to resonances close to μ that require a smaller (and opposite) energy gain than ΔE to generate current from R to L . Interestingly, features that look similar in the generated current and the injected heat, like, e.g., the current suppression for fixed x and for fixed $d - x$, see vertical and horizontal noises in Figs. 3(a) and 3(b), have very different noises, as shown in Fig. 4. Indeed S_{II} is maximal along the vertical ones (for fixed $d - x$) and minimal along the horizontal (fixed x), see Fig. 4(a). This asymmetry, caused by the finite ΔE , is much less evident in the fluctuations of the injected

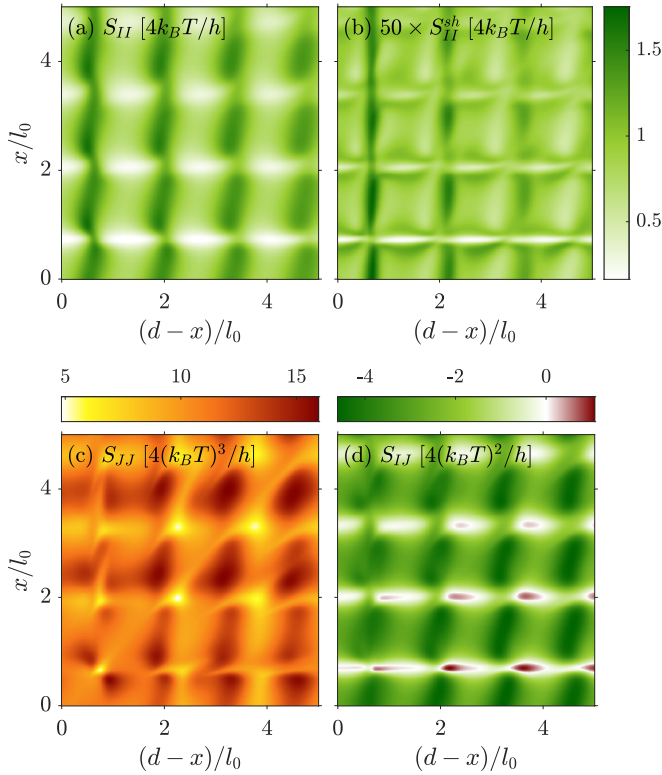


FIG. 4. (a) Particle current noise and (b) its shot contribution at terminal R , (c) heat noise at terminal H , and (d) crosscorrelation between injected heat from H and particle current at R , for the same scenario and parameters of Fig. 3.

heat current, S_{JJ} , cf. Fig. 4(c). Though S_{II} is strongly dominated by the thermal contribution at these temperatures, the shot noise term is also sensitive to this feature, see Fig. 4(b). Note that S_{II}^{sh} is rapidly suppressed as the separation of the two scatterers increases. This is not the case of the mixed noise, which increases with the scatterers' separation, thus serving as an indicator of the tiny spots where the generated current changes sign in the long-wire regime, see Fig. 4(d). Let us mention that the noise S_{LL} shows the same features as S_{RR} reflected over the antidiagonal: i.e., maxima in the horizontal current suppressions, minima in the vertical ones (not shown). However, in the regions where the particle current is maximal, both contributions are roughly the same, so it does not matter which one we chose for the optimization.

In a real wire, the separation of the scatterers is typically fixed, while the position of the resonant energies can be controlled with plunger gates [11]. Figures 5(a) and 5(b) show the generated current and the injected heat as functions of the QD energy difference ΔE and the position of the tip, x , for a fixed distance $d = 5l_0$. The sign of the current is mainly determined by the sign of ΔE , as expected, see also Fig. 5(c). However, for small differences, the interference induced by the position of the tip is able to reverse the sign of the current. At $\Delta E = 0$, where a thermalized 2DEG thermocouple would be electron-hole symmetric (and hence $I = 0$ [40]), the scattering at the hot tip is able to induce an oscillating current, as shown explicitly in Fig. 5(c). Note the expected symmetry $X_I(x, \Delta E) = -X_I(d-x, -\Delta E)$ is fulfilled both for I_R and J_H .

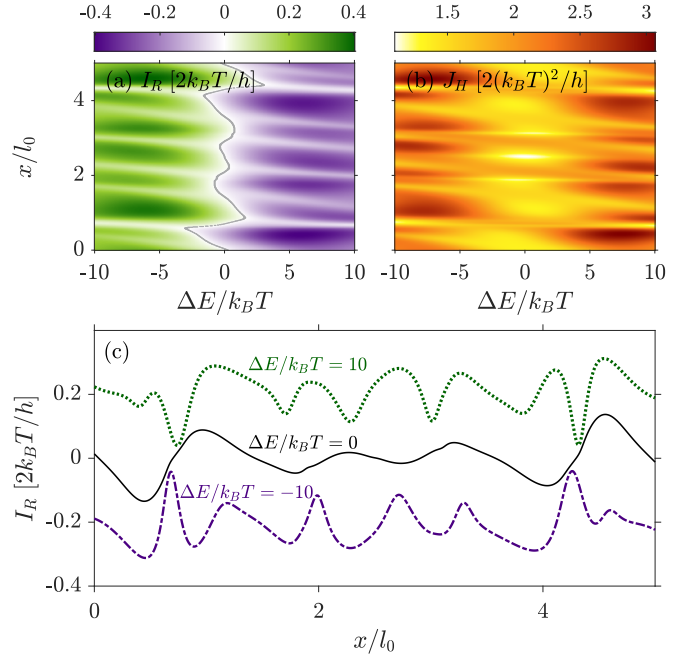


FIG. 5. (a) Generated zero bias thermoelectric current, I_R , and (b) injected heat current, J_H , as functions of x and ΔE in the QD case. The dashed line in (a) marks the condition $I = 0$. (c) Cuts of the current in (a) for fixed ΔE , as indicated. Parameters: $d = 5l_0$, $\epsilon = 0.5$, $\Gamma = 2k_B T$, $\mu = 20k_B T$, $\Delta T/T = 1$.

The maxima of the generated current and the injected heat occur at different positions, however, in both cases they are in the region around $\Delta E \sim 5 - 10k_B T$, for $T_H = 2T$, see Figs. 5(a) and 5(b). At higher energies of the resonant levels, the thermal fluctuations of terminal H become negligible and both currents are suppressed. This result, also depends strongly on other parameters, in particular, the linewidth, Γ (here we considered $\Gamma = 2k_B T$ which maximizes the response, as will be shown later). For this reason, it is useful to find the optimal parameters that enhance the thermoelectric properties of the device. In what follows, we will do so for the two configurations consisting of QD and DQD scatterers. We will (quite arbitrarily) consider $\mu = 20k_B T$ and $\Delta T/T = 1$, except where explicitly stated.

IV. PERFORMANCE OPTIMIZATION

In the sections above, transport was induced by the hot terminal, with the electric current flowing at zero bias. To generate a finite power, this current needs to flow against an electrochemical potential difference. In the following, we focus on the performance of such a heat engine. There are different ways one can optimize it. Traditionally, researchers have been interested in getting either the highest efficiency [6], which usually comes along with tiny generated powers, or the efficiency at maximum power, which may be a good strategy when one is not limited by the amount of generated power and wants to minimize the cost of the used resources, e.g., in power plants [118]. A different strategy is to maximize the efficiency for a given value of power that one needs to use [7], for instance, to run a particular device with an on-chip

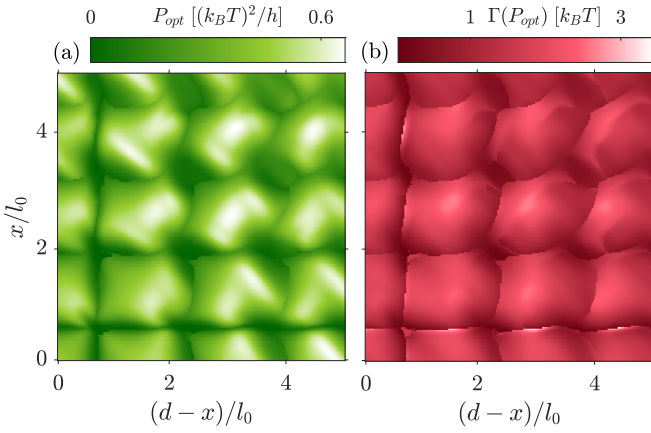


FIG. 6. Optimization procedure: the parameters of the QD system, Λ_{QD} , are optimized for each configuration $(d-x, x)$ to obtain the maximum power, P_{opt} , shown in (a) for fixed $\Delta T/T = 1$ and $\mu = 20k_{\text{B}}T$. (b) Obtained values for Γ .

energy harvester. Depending on the chosen procedure, the desired properties of the engine are different: sharp resonant transmissions give maximal efficiencies, while boxcar-shaped transmissions maximize the efficiency for a given power.

In a mesoscopic sample as ours, the generated power is expected to be a small quantity. Also, as we discuss below, the different quantities cannot be optimized simultaneously. Hence, we chose to optimize the parameters that give the maximal power and compare the resulting performance quantifiers (power, efficiency, and noise) for the different models with QD and DQD scatterers and the QD-th model of Ref. [40].

Let us first describe the procedure to find optimal configurations of the device in detail. For fixed μ and ΔT , we define the function $P(x, d, \Lambda_q)$ which gives the extracted power for given distances x and d and a particular set of parameters, Λ_q , we want to optimize: $\Lambda_{\text{QD}} = \{\Gamma, \Delta E, \Delta\mu, \epsilon\}$, $\Lambda_{\text{DQD}} = \{\Gamma, \lambda, \Delta E, \Delta\mu, \epsilon\}$, and $\Lambda_{\text{QD-th}} = \{\Gamma, \Delta E, \Delta\mu\}$, in each case. Note that Λ_q fully describe the properties of the scatterers. Then, the function $-P(x, d, \Lambda_q)$ is numerically minimized with respect to the chosen set. This is repeated for multiple combinations of distances, as illustrated in Fig. 6(a) for the QD case, where $P_{\text{opt}} = P(\Lambda_{\text{QD}}^{\text{opt}})$ is the value of the extracted power for the parameters obtained after the minimization, $\Lambda_{\text{QD}}^{\text{opt}}$. As a representative value, we show in Fig. 6(b) the obtained values of Γ_{opt} that optimize power at each pair of distances $(d-x, x)$, which is found to vary around a few times $k_{\text{B}}T$. Note that for the distances where the currents are suppressed (see Fig. 3) no set of parameters is able to generate any substantial power. In these regions, the destructive interference between the two scatterers (strongly dependent on x and d) dominates (the absence of) transport. Furthermore, for the areas where P_{opt} is maximum, the optimal values for the parameters (here only shown for Γ) only vary smoothly.

Our numerical minimization searches for local minima around a guessed set of parameters with Γ , ΔE , and $\Delta\mu$ of the order of $k_{\text{B}}T$, and for a strongly coupled tip, $\epsilon \approx 1/2$. The obtained parameters give us information about how the optimal transmission probabilities result from the combination of the interference patterns and the properties of the scatterers. The

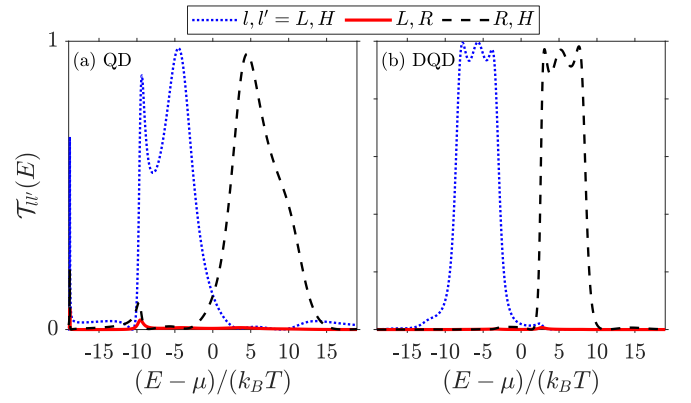


FIG. 7. Energy dependence of the (a) QD and (b) DQD transmission probabilities when parameters are chosen to optimize the extracted power at a particular position of the tip having a maximum of P : (a) $d = 5.6l_0$, $x = 2.6l_0$, giving $\Lambda_{\text{QD}}/k_{\text{B}}T = \{2.3, 11, 1.6, 0.5/k_{\text{B}}T\}$, and (b) $d = 6.4l_0$, $x = 6.2l_0$, with $\Lambda_{\text{DQD}}/k_{\text{B}}T = \{3.1, 2.1, 11.7, 2.2, 0.43/k_{\text{B}}T\}$.

resulting transmissions are plotted in Fig. 7 for the QD and DQD cases for two different $(d-x, x)$ configurations chosen to have a maximal power. In both cases, we observe that the transmission probabilities between the conductor terminals and H are broad peaks with sharp borders. This is particularly evident in the DQD case, for which both $\mathcal{T}_{LH}(E)$ and $\mathcal{T}_{RH}(E)$ approach a boxcar function of width $\sim 8k_{\text{B}}T$ and centered around $E - \mu \approx \Delta E/2 \sim 6k_{\text{B}}T$. Furthermore, as discussed in Sec. II C, destructive interference almost completely cancels $\mathcal{T}_{LR}(E)$, confirming the detrimental contribution of elastic transport between the two conductor terminals. Clearly, electrons that are not absorbed by the tip do not contribute to the thermoelectric current.

The chosen performance quantifiers for the different configurations (QD, DQD, and QD-th) are shown in Fig. 8 by optimizing the parameters as ΔT is increased: P_{opt} , $\eta^* \equiv \eta(\Lambda_{\text{opt}})$ and $1/F^*$, with $F^* \equiv F(\Lambda_{\text{opt}})$. It shows that indeed the DQD setting performs better in terms of a larger power and efficiency, as well as a less noisy output current. The effect of the coherent coupling to H via the tip also results in being advantageous in the comparison of the QD and the QD-th setups. This is a clear manifestation of the improvement of considering the interference patterns that modulate the shape of the scattering resonances. The fact that the DQD is closer to a boxcar function than the QD is not totally surprising, as these transmissions have been proposed to be the asymptotic limit of arrays of QDs [7,74]. In our case, the Fabry-Pérot-like resonance between the DQD and the tip plays the role of an additional QD. An advantage of our setup is that, while one can only have control of the system parameters (ϵ_α , Γ , and λ) up to some extent in a real experiment, sample imperfections can be compensated with an appropriate tuning of the tip position. It is expected that adding more QDs will help the optimization. However, this would come at the expense of increasing the system complexity and decreasing the degree of control.

As expected, the maximal power, in general, increases with ΔT . Note that Fig. 8(a) normalizes it with the power bound, cf. Eq. (17), which increases quadratically. For small temper-

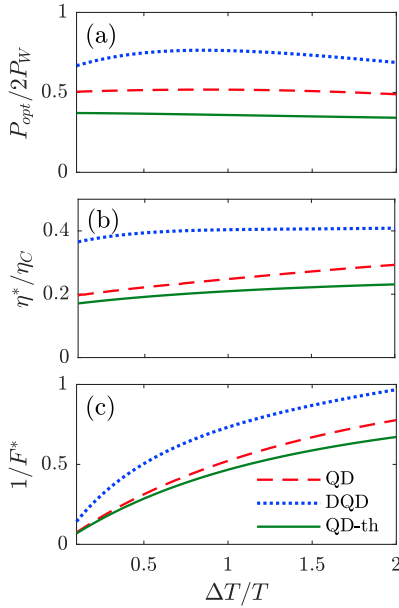


FIG. 8. Performance quantifiers: (a) P_{opt} , (b) η^* , and (c) $1/F^*$, as functions of the temperature difference for the QD (red dashed) and DQD (blue dotted) cases, compared with the QD-th (green full lines). The parameters are optimized for each system to extract maximum power at each ΔT and fixed $\mu = 20k_B T$, with x and d being the same as in Figs. 7(a) and 7(b) for the QD and DQD, respectively.

ature difference, P_{opt} increases as $(\Delta T)^\gamma$, with $\gamma > 2$ in the DQD, getting closest to $2P_W$ around $\Delta T \approx T$. In the other two cases, this ratio does not change appreciably, indicating $\gamma \approx 2$, see Fig. 8(a). Differently, the efficiency increases at the same rate as the Carnot efficiency for the DQD, while the QD and QD-th cases both increase their efficiency with ΔT , see Fig. 8(b).

We then chose the temperature difference $\Delta T = T$, and compare the performance of the different models (properly optimized) as a function of the applied bias. The results are shown in Figs. 9(a)–9(c). Again, the DQD case outperforms the other cases for all quantifiers. However, power and efficiency are very similar for QD and DQD at low voltages. This is not the case for the inverse Fano factor, for which QD and QD-th give lower values. As anticipated in Sec. IID, the Fano factor changes from sub to super-Poissonian with $\Delta\mu$, see Fig. 9(c). Let us note that the DQD configuration seems to be beneficial for the increase of $1/F$ when compared with sharp step transmissions (with, e.g., a quantum point contact) in two-terminal thermoelectrics [88]. It is also useful to plot the power and efficiency relation as voltage is tuned between $\Delta\mu = 0$ and the stopping voltage, see Fig. 9(d). In all cases, the resulting elongated lasso diagrams involve that the maximum power and maximum efficiency points occur for not very different voltages. Remarkably, the efficiency of the DQD case reaches high values $\eta > 0.4\eta_C$, not far from the maximal efficiency bound, η_W , (calculated following Ref. [112]) for the same voltage (around $0.6\eta_C$).

Figure 10 gives a more complete description of how the QD and DQD configurations perform as the system is brought out of equilibrium by increasing $\Delta\mu$ and ΔT . The regions in which power and efficiency are maximal roughly coincide,

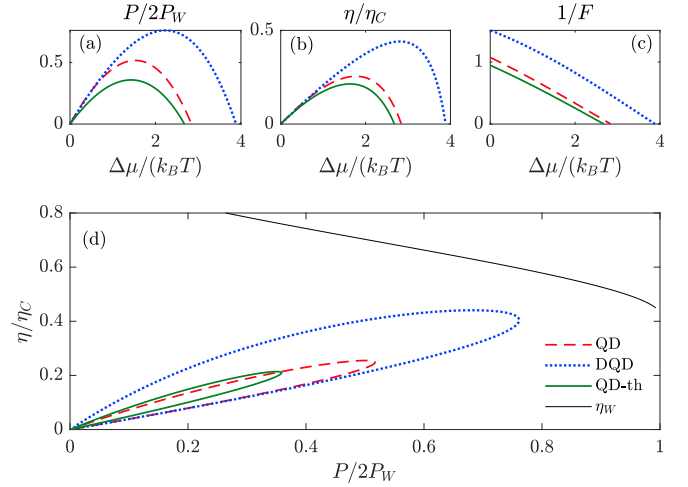


FIG. 9. Performance quantifiers: (a) P , (b) η , and (c) $1/F$, as functions of $\Delta\mu$ for the QD (red dashed) and DQD (blue dotted) cases, compared with the QD-th one (green full lines). The parameters are those that maximize the extracted power at $\Delta T/T = 1$ and $\mu = 20k_B T$ in each case: those of Fig. 7 for the QD and DQD cases, and $\Gamma = 1.6k_B T$ and $\Delta E = 9k_B T$ for the QD-th. (d) Lasso diagrams relating P and η as $\Delta\mu$ is varied from 0 and the corresponding stopping voltage. The black curve indicates the calculated bound for efficiency at given power output, η_W .

though the maxima do not occur for the same configurations, see Figs. 10(a), 10(b), 10(e), and 10(f). In this sense, it does not seem complicated to find a reasonable compromise to get a powerful and efficient heat engine. Reducing the output noise at the same time is more challenging, as $1/F$ increases in the region with small $\Delta\mu$ and high ΔT , where both P and η are strongly suppressed, see Figs. 10(c) and 10(g). Panels in Figs. 10(d) and 10(h) may be helpful for that task. They can be understood as plotting $1/F$ in a compilation of all the lasso diagrams [like those in Fig. 9(d)] for all ΔT giving a thermoelectric response. They clearly show that the signal-to-noise ratio is actually larger in the region where P and η are smallest. One can also see that for a given efficiency, $1/F$ increases with P . On the contrary, for a given power, $1/F$ decreases with η . Hence, to find a regular energy harvester, it seems more convenient to operate the system at higher powers even if efficiency is slightly compromised. Note that the DQD allows one to do so with a smaller decrease in the engine efficiency, as well as with an overall larger P and η approaching $\eta_C/2$.

V. CONCLUSIONS

We have investigated the role of internal coherence in the propagation of electrons through mesoscopic three-terminal energy harvesters. For this, we couple an isothermal two-terminal conductor to a heat bath via a coherent beam splitter, which allows for interference in the conductor-bath coupling. Experimentally, this can consist of a one-dimensional semiconductor quantum wire, with the QDs formed by conveniently stopping the growth process to include tunneling barriers [32,119]. Side plunger gates can be then added to tune the QD energy levels. The coupling can be due to the tip of a

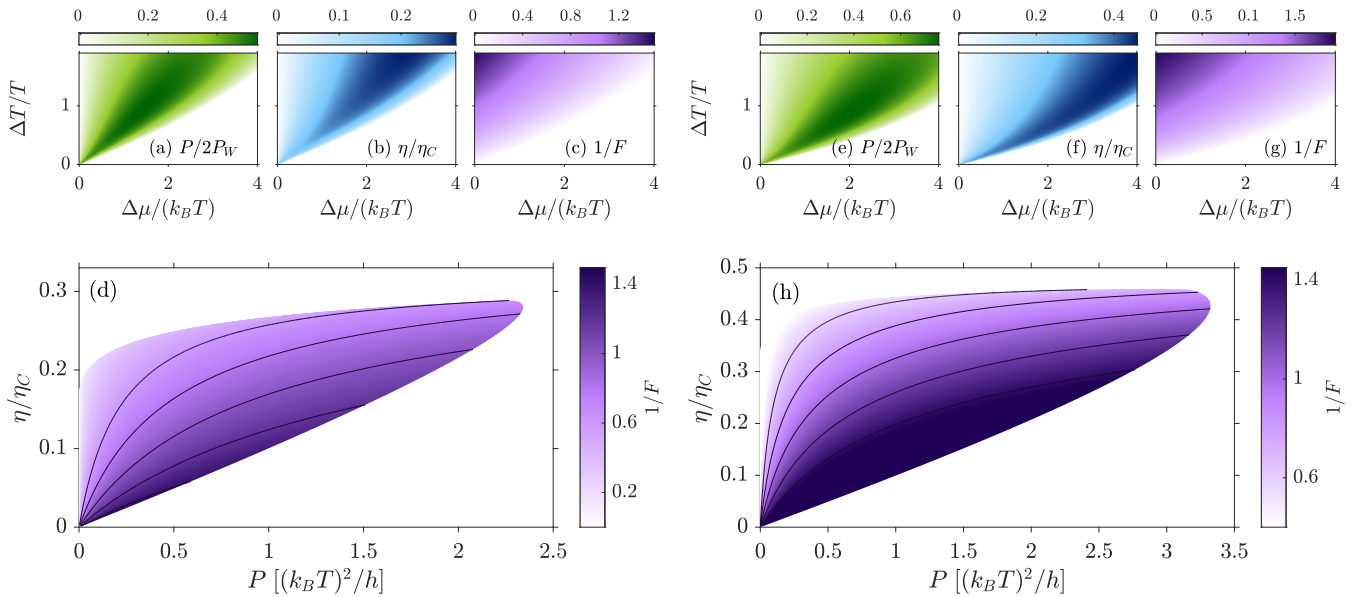


FIG. 10. Performance quantifiers for (a)–(d) the QD and (e)–(h) the DQD configurations as functions of applied bias and temperature difference: (a), (e) Extracted power normalized by the power bound P_W ; (b), (f) efficiency and (c), (g) inverse Fano factor. The parameters are those of Fig. 7(a) for the QD case and of Fig. 7(b) for the QD, chosen in both cases to maximize the power for fixed $\Delta T/T = 1$ and $\mu = 20k_B T$. (d), (h) Trade-off relation among P , η , and $1/F$ for different values of $\Delta\mu$ and ΔT (similar to the lasso diagrams of Fig. 9). Lines are shown along which $1/F$ is constant.

scanning probe [66,67,120,121], hence introducing a mechanism to control the interference pattern. One-dimensional channels with QDs can also be patterned in two-dimensional materials [69] or two-dimensional electron gases, see, e.g., Refs. [122,123]. The latter are unfortunately less accessible by a movable tip, though a hot third terminal can be connected by a quantum point contact at a fixed position of the wire [11,124].

We find that the combination of resonant tunneling scatterers between the tip and the conductor terminals and modulated internal interferences considerably increases both the generated power and efficiency with respect to related configurations involving only one of these effects [17,40]. This is due to the particular spectral dependence of the resulting transmission probabilities between the three terminals. Our results show that improving the (nonlocal) thermoelectric response requires the suppression of elastic transport along the conductor, which results from destructive interference for certain positions of the tip. On top of that, optimal configurations are found where the coupling between the conductor terminals and the tip occurs via broadband filters, in line with related proposals [7]. Configurations with DQD scatterers give transmission probabilities which approach sharp boxcar functions, optimizing the heat engine performance in terms of the generated power, the efficiency, and the output signal to noise ratio.

As expected, one needs to find a compromise between producing the highest power and doing it at the highest efficiency. However, we observe the detriment in either case is not big. Though the signal-to-noise ratio is mostly enhanced in the regions with low power and low efficiency, it is found to improve for configurations with increasing power for a fixed

efficiency. On the contrary, for a given power production, increasing the efficiency comes with the cost of noisier currents.

Tunable internal interferences hence introduce a valuable way to control the properties of quantum heat engines via the coherent control of transport spectral properties. Here we discussed energy harvesting, but it will also affect absorption refrigerators [125] as well, where heat autocorrelations will be important. Additional control may be achieved in interferometers that combine kinetic phases with magnetic field effects [14] or additional degrees of freedom like, e.g., spin [126].

Concerning the noise, auto-, and crosscorrelations are sensitive to Coulomb interaction effects that are not treated at the mean-field level. In particular, super-Poissonian autocorrelations are expected in the Coulomb blockade regime [84,127], which may arise in the weakly coupled short wire limit. This effect is naively expected to be detrimental to the performance of the engine for increasing the noise, at the same time reducing the current.

We have assumed here a phenomenological approach based on simple but physically relevant scattering matrices describing resonant tunneling scatterers in a one-dimensional elastic conductor, considering that otherwise energy-dependent scattering only emerges due to phase coherence. Possible additional contributions due to, e.g., the effect of disorder in the wire potential [109] or of more involved energy dependence in the transmission coefficients simply add a level of complexity to the optimization problem but do not compromise our general conclusions. Extensions of our paper including the effect of dephasing [17] or of inelastic scattering due to the (typically weak) interaction with a thermal bath [110,128] (phononic or electromagnetic environments) are interesting questions to be addressed in future works.

ACKNOWLEDGMENTS

We thank M. Acciai for useful comments on the paper, and acknowledge funding from the Ramón y Cajal Program No. RYC-2016-20778 and the Spanish Ministerio de Ciencia e Innovación via Grants No. PID2019-110125GB-I00 and No. PID2022-142911NB-I00, and through the María de Maeztu Programme for Units of Excellence in R&D No. CEX2018-000805-M.

APPENDIX: DOUBLE QUANTUM DOT SCATTERING MATRIX

The transmission and reflection amplitudes for a DQD are obtained via noninteracting single-particle Green's functions [1,129]. We model the scattering region defined by the coupled QDs by a two-site Hamiltonian with same level energy, ε , and coherent tunneling λ :

$$\hat{H}_{\text{DQD}} = \begin{pmatrix} \varepsilon & \lambda \\ \lambda & \varepsilon \end{pmatrix}. \quad (\text{A1})$$

Coupling to left (L') and right (R') one-dimensional semi-infinite leads enters in the calculation of the retarded Green's

function via self-energies $\hat{\Sigma}_{L'}^r, \hat{\Sigma}_{R'}^r$,

$$\hat{G}_S^r(E) = [E\hat{I} - \hat{H}_{\text{DQD}} - \hat{\Sigma}_{L'}^r - \hat{\Sigma}_{R'}^r]^{-1}, \quad (\text{A2})$$

with the identity matrix \hat{I} . In the wide-band limit and for symmetric coupling to the leads, the self-energy matrices read

$$\hat{\Sigma}_{L'}^r = \begin{pmatrix} -i\Gamma/2 & 0 \\ 0 & 0 \end{pmatrix} \quad \text{and} \quad \hat{\Sigma}_{R'}^r = \begin{pmatrix} 0 & 0 \\ 0 & -i\Gamma/2 \end{pmatrix}, \quad (\text{A3})$$

where $\Gamma = \hbar v$, v being the velocity of the electrons in the leads. Self-energies beyond the wide-band limit would introduce an additional modulation to the scattering coefficients that can be compensated by the position of the tip or the QD levels [130]. Substituting Eqs. (A1) and (A3) in Eq. (A2), we obtain the desired Green's function of the system:

$$\hat{G}_S^r(E) = \frac{1}{(E - \varepsilon + i\Gamma/2)^2 - \lambda^2} \begin{pmatrix} E - \varepsilon + i\Gamma/2 & \lambda \\ \lambda & E - \varepsilon + i\Gamma/2 \end{pmatrix}. \quad (\text{A4})$$

The scattering matrix can now be calculated from the retarded Green's function using the Fisher-Lee relation [1,131]:

$$\mathcal{S}(E) = \hat{I} - i\hbar v \hat{G}_S^r(E), \quad (\text{A5})$$

the elements of which are the transmission and reflection amplitudes of Eq. (9).

-
- [1] S. Datta, *Electronic Transport in Mesoscopic Systems* (Cambridge University Press, Cambridge, England, UK, 1995).
- [2] Y. V. Nazarov and Y. M. Blanter, *Quantum Transport: Introduction to Nanoscience* (Cambridge University Press, Cambridge, England, UK, 2009).
- [3] T. Ihn, *Semiconductor Nanostructures: Quantum States and Electronic Transport* (Oxford University Press, Oxford, England, UK, 2009).
- [4] L. D. Hicks and M. S. Dresselhaus, Effect of quantum-well structures on the thermoelectric figure of merit, *Phys. Rev. B* **47**, 12727 (1993).
- [5] L. D. Hicks and M. S. Dresselhaus, Thermoelectric figure of merit of a one-dimensional conductor, *Phys. Rev. B* **47**, 16631 (1993).
- [6] G. D. Mahan and J. O. Sofo, The best thermoelectric, *Proc. Natl. Acad. Sci. USA* **93**, 7436 (1996).
- [7] R. S. Whitney, Most efficient quantum thermoelectric at finite power output, *Phys. Rev. Lett.* **112**, 130601 (2014).
- [8] B. Sothmann, R. Sánchez, and A. N. Jordan, Thermoelectric energy harvesting with quantum dots, *Nanotechnology* **26**, 032001 (2015).
- [9] G. Benenti, G. Casati, K. Saito, and R. S. Whitney, Fundamental aspects of steady-state conversion of heat to work at the nanoscale, *Phys. Rep.* **694**, 1 (2017).
- [10] M. Josefsson, A. Svilans, A. M. Burke, E. A. Hoffmann, S. Fahlvik, C. Thelander, M. Leijnse, and H. Linke, A quantum-dot heat engine operating close to the thermodynamic efficiency limits, *Nat. Nanotechnol.* **13**, 920 (2018).
- [11] G. Jaliel, R. K. Puddy, R. Sánchez, A. N. Jordan, B. Sothmann, I. Farrer, J. P. Griffiths, D. A. Ritchie, and C. G. Smith, Experimental realization of a quantum dot energy harvester, *Phys. Rev. Lett.* **123**, 117701 (2019).
- [12] P. P. Hofer and B. Sothmann, Quantum heat engines based on electronic Mach-Zehnder interferometers, *Phys. Rev. B* **91**, 195406 (2015).
- [13] P. Samuelsson, S. Kheradsoud, and B. Sothmann, Optimal quantum interference thermoelectric heat engine with edge states, *Phys. Rev. Lett.* **118**, 256801 (2017).
- [14] G. Haack and F. Giazotto, Efficient and tunable Aharonov-Bohm quantum heat engine, *Phys. Rev. B* **100**, 235442 (2019).
- [15] G. Haack and F. Giazotto, Nonlinear regime for enhanced performance of an Aharonov-Bohm heat engine, *AVS Quantum Sci.* **3**, 046801 (2021).
- [16] L. Vannucci, F. Ronetti, G. Dolcetto, M. Carrega, and M. Sassetti, Interference-induced thermoelectric switching and heat rectification in quantum Hall junctions, *Phys. Rev. B* **92**, 075446 (2015).
- [17] R. Sánchez, C. Gorini, and G. Fleury, Extrinsic thermoelectric response of coherent conductors, *Phys. Rev. B* **104**, 115430 (2021).
- [18] C. M. Finch, V. M. García-Suárez, and C. J. Lambert, Giant thermopower and figure of merit in single-molecule devices, *Phys. Rev. B* **79**, 033405 (2009).
- [19] O. Karlström, H. Linke, G. Karlström, and A. Wacker, Increasing thermoelectric performance using coherent transport, *Phys. Rev. B* **84**, 113415 (2011).
- [20] G. Gómez-Silva, O. Ávalos Ovando, M. L. Ladrón de Guevara, and P. A. Orellana, Enhancement of thermoelectric efficiency and violation of the Wiedemann-Franz law due to Fano effect, *J. Appl. Phys.* **111**, 053704 (2012).

- [21] S. Hershfield, K. A. Muttalib, and B. J. Nartowt, Nonlinear thermoelectric transport: A class of nanodevices for high efficiency and large power output, *Phys. Rev. B* **88**, 085426 (2013).
- [22] P. N. Butcher, Thermal and electrical transport formalism for electronic microstructures with many terminals, *J. Phys.: Condens. Matter* **2**, 4869 (1990).
- [23] F. Mazza, R. Bosisio, G. Benenti, V. Giovannetti, R. Fazio, and F. Taddei, Thermoelectric efficiency of three-terminal quantum thermal machines, *New J. Phys.* **16**, 085001 (2014).
- [24] R. Sánchez and M. Büttiker, Optimal energy quanta to current conversion, *Phys. Rev. B* **83**, 085428 (2011).
- [25] H. Thierschmann, R. Sánchez, B. Sothmann, F. Arnold, C. Heyn, W. Hansen, H. Buhmann, and L. W. Molenkamp, Three-terminal energy harvester with coupled quantum dots, *Nat. Nanotechnol.* **10**, 854 (2015).
- [26] A.-M. Daré and P. Lombardo, Powerful Coulomb-drag thermoelectric engine, *Phys. Rev. B* **96**, 115414 (2017).
- [27] N. Walldorf, A.-P. Jauho, and K. Kaasbjerg, Thermoelectrics in Coulomb-coupled quantum dots: Cotunneling and energy-dependent lead couplings, *Phys. Rev. B* **96**, 115415 (2017).
- [28] O. Entin-Wohlman, Y. Imry, and A. Aharony, Three-terminal thermoelectric transport through a molecular junction, *Phys. Rev. B* **82**, 115314 (2010).
- [29] J.-H. Jiang, O. Entin-Wohlman, and Y. Imry, Thermoelectric three-terminal hopping transport through one-dimensional nanosystems, *Phys. Rev. B* **85**, 075412 (2012).
- [30] R. Bosisio, G. Fleury, J.-L. Pichard, and C. Gorini, Nanowire-based thermoelectric ratchet in the hopping regime, *Phys. Rev. B* **93**, 165404 (2016).
- [31] H. Zhou, G. Zhang, J.-S. Wang, and Y.-W. Zhang, Three-terminal interface as a thermoelectric generator beyond the Seebeck effect, *Phys. Rev. B* **101**, 235305 (2020).
- [32] S. Dorsch, A. Svilans, M. Josefsson, B. Goldozian, M. Kumar, C. Thelander, A. Wacker, and A. Burke, Heat driven transport in serial double quantum dot devices, *Nano Lett.* **21**, 988 (2021).
- [33] S. Dorsch, S. Fahlvik, and A. Burke, Characterization of electrostatically defined bottom-heated InAs nanowire quantum dot systems, *New J. Phys.* **23**, 125007 (2021).
- [34] C. Bergenfeldt, P. Samuelsson, B. Sothmann, C. Flindt, and M. Büttiker, Hybrid microwave-cavity heat engine, *Phys. Rev. Lett.* **112**, 076803 (2014).
- [35] B. Sothmann, R. Sánchez, A. N. Jordan, and M. Büttiker, Rectification of thermal fluctuations in a chaotic cavity heat engine, *Phys. Rev. B* **85**, 205301 (2012).
- [36] F. Hartmann, P. Pfeffer, S. Höfling, M. Kamp, and L. Worschech, Voltage fluctuation to current converter with Coulomb-coupled quantum dots, *Phys. Rev. Lett.* **114**, 146805 (2015).
- [37] B. Roche, P. Roulleau, T. Jullien, Y. Jompol, I. Farrer, D. A. Ritchie, and D. C. Glattli, Harvesting dissipated energy with a mesoscopic ratchet, *Nat. Commun.* **6**, 6738 (2015).
- [38] T. E. Humphrey and H. Linke, Reversible thermoelectric nanomaterials, *Phys. Rev. Lett.* **94**, 096601 (2005).
- [39] D. Sánchez and L. Serra, Thermoelectric transport of mesoscopic conductors coupled to voltage and thermal probes, *Phys. Rev. B* **84**, 201307(R) (2011).
- [40] A. N. Jordan, B. Sothmann, R. Sánchez, and M. Büttiker, Powerful and efficient energy harvester with resonant-tunneling quantum dots, *Phys. Rev. B* **87**, 075312 (2013).
- [41] B. Sothmann, R. Sánchez, A. N. Jordan, and M. Büttiker, Powerful energy harvester based on resonant-tunneling quantum wells, *New J. Phys.* **15**, 095021 (2013).
- [42] G. Fleury, C. Gorini, and R. Sánchez, Scanning probe-induced thermoelectrics in a quantum point contact, *Appl. Phys. Lett.* **119**, 043101 (2021).
- [43] S. Donsa, S. Andergassen, and K. Held, Double quantum dot as a minimal thermoelectric generator, *Phys. Rev. B* **89**, 125103 (2014).
- [44] R. T. Ross and A. J. Nozik, Efficiency of hot-carrier solar energy converters, *J. Appl. Phys.* **53**, 3813 (1982).
- [45] P. Würfel, Solar energy conversion with hot electrons from impact ionisation, *Sol. Energy Mater. Sol. Cells* **46**, 43 (1997).
- [46] P. Würfel, A. S. Brown, T. E. Humphrey, and M. A. Green, Particle conservation in the hot-carrier solar cell, *Prog. Photovoltaics Res. Appl.* **13**, 277 (2005).
- [47] L. Tesser, R. S. Whitney, and J. Splettstoesser, Thermodynamic performance of hot-carrier solar cells: A quantum transport model, *Phys. Rev. Appl.* **19**, 044038 (2023).
- [48] P. Machon, M. Eschrig, and W. Belzig, Nonlocal thermoelectric effects and nonlocal Onsager relations in a three-terminal proximity-coupled superconductor-ferromagnet device, *Phys. Rev. Lett.* **110**, 047002 (2013).
- [49] Z. Cao, T.-F. Fang, L. Li, and H.-G. Luo, Thermoelectric-induced unitary Cooper pair splitting efficiency, *Appl. Phys. Lett.* **107**, 212601 (2015).
- [50] R. Sánchez, P. Buset, and A. L. Yeyati, Cooling by Cooper pair splitting, *Phys. Rev. B* **98**, 241414(R) (2018).
- [51] R. Hussein, M. Governale, S. Kohler, W. Belzig, F. Giazotto, and A. Braggio, Nonlocal thermoelectricity in a Cooper-pair splitter, *Phys. Rev. B* **99**, 075429 (2019).
- [52] N. S. Kirsanov, Z. B. Tan, D. S. Golubev, P. J. Hakonen, and G. B. Lesovik, Heat switch and thermoelectric effects based on Cooper-pair splitting and elastic cotunneling, *Phys. Rev. B* **99**, 115127 (2019).
- [53] Z. B. Tan, A. Laitinen, N. S. Kirsanov, A. Galda, V. M. Vinokur, M. Haque, A. Savin, D. S. Golubev, G. B. Lesovik, and P. J. Hakonen, Thermoelectric current in a graphene Cooper pair splitter, *Nat. Commun.* **12**, 1 (2021).
- [54] F. Mazza, S. Valentini, R. Bosisio, G. Benenti, V. Giovannetti, R. Fazio, and F. Taddei, Separation of heat and charge currents for boosted thermoelectric conversion, *Phys. Rev. B* **91**, 245435 (2015).
- [55] S. M. Tabatabaei, D. Sánchez, A. L. Yeyati, and R. Sánchez, Nonlocal quantum heat engines made of hybrid superconducting devices, *Phys. Rev. B* **106**, 115419 (2022).
- [56] R. López, J. S. Lim, and K. W. Kim, Optimal superconducting hybrid machine, *Phys. Rev. Res.* **5**, 013038 (2023).
- [57] G. Granger, J. P. Eisenstein, and J. L. Reno, Observation of chiral heat transport in the quantum Hall regime, *Phys. Rev. Lett.* **102**, 086803 (2009).
- [58] S.-G. Nam, E. H. Hwang, and H.-J. Lee, Thermoelectric detection of chiral heat transport in graphene in the quantum Hall regime, *Phys. Rev. Lett.* **110**, 226801 (2013).
- [59] R. Sánchez, B. Sothmann, and A. N. Jordan, Chiral thermoelectrics with quantum Hall edge states, *Phys. Rev. Lett.* **114**, 146801 (2015).

- [60] G. Blasi, F. Taddei, L. Arrachea, M. Carrega, and A. Braggio, Nonlocal thermoelectricity in a superconductor–topological-insulator–superconductor junction in contact with a normal-metal probe: Evidence for helical edge states, *Phys. Rev. Lett.* **124**, 227701 (2020).
- [61] G. Blasi, F. Taddei, L. Arrachea, M. Carrega, and A. Braggio, Nonlocal thermoelectricity in a topological Andreev interferometer, *Phys. Rev. B* **102**, 241302(R) (2020).
- [62] A. Braggio, M. Carrega, B. Sothmann, and R. Sánchez, Nonlocal thermoelectric detection of interaction and correlations in edge states, [arXiv:2307.09410](https://arxiv.org/abs/2307.09410).
- [63] M. Büttiker, Chemical potential oscillations near a barrier in the presence of transport, *Phys. Rev. B* **40**, 3409 (1989).
- [64] T. Gramespacher and M. Büttiker, Nanoscopic tunneling contacts on mesoscopic multiprobe conductors, *Phys. Rev. B* **56**, 13026 (1997).
- [65] T. Gramespacher and M. Büttiker, Local non-equilibrium distribution of charge carriers in a phase-coherent conductor, *Comptes Rendus de l'Académie des Sciences - Series IIB - Mechanics-Physics-Astronomy* **327**, 877 (1999).
- [66] J. Fast, E. Barrigon, M. Kumar, Y. Chen, L. Samuelson, M. Borgström, A. Gustafsson, S. Limpert, A. Burke, and H. Linke, Hot-carrier separation in heterostructure nanowires observed by electron-beam induced current, *Nanotechnology* **31**, 394004 (2020).
- [67] N. Gächter, F. Könemann, M. Sistani, M. G. Bartmann, M. Sousa, P. Staudinger, A. Lugstein, and B. Gotsmann, Spatially resolved thermoelectric effects in *operando* semiconductor–metal nanowire heterostructures, *Nanoscale* **12**, 20590 (2020).
- [68] J. Park, G. He, R. M. Feenstra, and A.-P. Li, Atomic-scale mapping of thermoelectric power on graphene: Role of defects and boundaries, *Nano Lett.* **13**, 3269 (2013).
- [69] A. Harzheim, J. Spiece, C. Evangeli, E. McCann, V. Falko, Y. Sheng, J. H. Warner, G. A. D. Briggs, J. A. Mol, P. Gehring, and O. V. Kolosov, Geometrically enhanced thermoelectric effects in graphene nanoconstrictions, *Nano Lett.* **18**, 7719 (2018).
- [70] B. Brun, F. Martins, S. Faniel, A. Cavanna, C. Ulysse, A. Ouerghi, U. Gennser, D. Mailly, P. Simon, S. Huant, M. Sanquer, H. Sellier, V. Bayot, and B. Hackens, Thermoelectric scanning-gate interferometry on a quantum point contact, *Phys. Rev. Appl.* **11**, 034069 (2019).
- [71] K. Yamamoto and N. Hatano, Thermodynamics of the mesoscopic thermoelectric heat engine beyond the linear-response regime, *Phys. Rev. E* **92**, 042165 (2015).
- [72] G. Bevilacqua, A. Cresti, G. Grosso, G. Menichetti, and G. P. Parravicini, Tutorial notes for the evaluation of thermoelectric quantum bounds in ideal nanostructures, [arXiv:2206.00294](https://arxiv.org/abs/2206.00294).
- [73] R. S. Whitney, Quantum coherent three-terminal thermoelectrics: Maximum efficiency at given power output, *Entropy* **18**, 208 (2016).
- [74] T. Ehrlich and G. Schaller, Broadband frequency filters with quantum dot chains, *Phys. Rev. B* **104**, 045424 (2021).
- [75] J. Behera, S. Bedkihal, B. K. Agarwalla, and M. Bandyopadhyay, Quantum coherent control of nonlinear thermoelectric transport in a triple-dot Aharonov-Bohm heat engine, *Phys. Rev. B* **108**, 165419 (2023).
- [76] G. Benenti, K. Saito, and G. Casati, Thermodynamic bounds on efficiency for systems with broken time-reversal symmetry, *Phys. Rev. Lett.* **106**, 230602 (2011).
- [77] O. Entin-Wohlman and A. Aharony, Three-terminal thermoelectric transport under broken time-reversal symmetry, *Phys. Rev. B* **85**, 085401 (2012).
- [78] K. Brandner and U. Seifert, Multi-terminal thermoelectric transport in a magnetic field: Bounds on Onsager coefficients and efficiency, *New J. Phys.* **15**, 105003 (2013).
- [79] K. Yamamoto, O. Entin-Wohlman, A. Aharony, and N. Hatano, Efficiency bounds on thermoelectric transport in magnetic fields: The role of inelastic processes, *Phys. Rev. B* **94**, 121402(R) (2016).
- [80] H. Zhou, J. Thingna, P. Hänggi, J.-S. Wang, and B. Li, Boosting thermoelectric efficiency using time-dependent control, *Sci. Rep.* **5**, 14870 (2015).
- [81] S. Ryu, R. López, L. Serra, and D. Sánchez, Beating Carnot efficiency with periodically driven chiral conductors, *Nat. Commun.* **13**, 2512 (2022).
- [82] Ya. M. Blanter and M. Büttiker, Shot noise in mesoscopic conductors, *Phys. Rep.* **336**, 1 (2000).
- [83] K. Kobayashi and M. Hashisaka, Shot noise in mesoscopic systems: From single particles to quantum liquids, *J. Phys. Soc. Jpn.* **90**, 102001 (2021).
- [84] R. Sánchez, B. Sothmann, A. N. Jordan, and M. Büttiker, Correlations of heat and charge currents in quantum-dot thermoelectric engines, *New J. Phys.* **15**, 125001 (2013).
- [85] A. Crépieux and F. Michelini, Mixed, charge and heat noises in thermoelectric nanosystems, *J. Phys.: Condens. Matter* **27**, 015302 (2014).
- [86] A. Crépieux and F. Michelini, Heat-charge mixed noise and thermoelectric efficiency fluctuations, *J. Stat. Mech.* (2016) 054015.
- [87] K. Ptaszyński, Coherence-enhanced constancy of a quantum thermoelectric generator, *Phys. Rev. B* **98**, 085425 (2018).
- [88] S. Kheradsoud, N. Dashti, M. Misiorny, P. P. Potts, J. Splettstoesser, and P. Samuelsson, Power, efficiency and fluctuations in a quantum point contact as steady-state thermoelectric heat engine, *Entropy* **21**, 777 (2019).
- [89] A. M. Timpanaro, G. Guarnieri, and G. T. Landi, Hyperaccurate thermoelectric currents, *Phys. Rev. B* **107**, 115432 (2023).
- [90] P. A. Erdman, A. Rolandi, P. Abiuso, M. Perarnau-Llobet, and F. Noé, Pareto-optimal cycles for power, efficiency and fluctuations of quantum heat engines using reinforcement learning, *Phys. Rev. Res.* **5**, L022017 (2023).
- [91] P. Eyméoud and A. Crépieux, Mixed electrical-heat noise spectrum in a quantum dot, *Phys. Rev. B* **94**, 205416 (2016).
- [92] J. Eriksson, M. Acciai, L. Tesser, and J. Splettstoesser, General bounds on electronic shot noise in the absence of currents, *Phys. Rev. Lett.* **127**, 136801 (2021).
- [93] S. Saryal, M. Gerry, I. Khait, D. Segal, and B. K. Agarwalla, Universal bounds on fluctuations in continuous thermal machines, *Phys. Rev. Lett.* **127**, 190603 (2021).
- [94] L. Tesser, M. Acciai, C. Spånslätt, J. Monsel, and J. Splettstoesser, Charge, spin, and heat shot noises in the absence of average currents: Conditions on bounds at zero and finite frequencies, *Phys. Rev. B* **107**, 075409 (2023).
- [95] S. Pugnetti, F. Dolcini, D. Bercioux, and H. Grabert, Electron tunneling into a quantum wire in the Fabry-Pérot regime, *Phys. Rev. B* **79**, 035121 (2009).
- [96] A. Crépieux, R. Guyon, P. Devillard, and T. Martin, Electron injection in a nanotube: Noise correlations and entanglement, *Phys. Rev. B* **67**, 205408 (2003).

- [97] M. V. Moskalets, *Scattering Matrix Approach to Non-Stationary Quantum Transport* (Imperial College Press, London, England, UK, 2011).
- [98] U. Sivan and Y. Imry, Multichannel Landauer formula for thermoelectric transport with application to thermopower near the mobility edge, *Phys. Rev. B* **33**, 551 (1986).
- [99] G. D. Guttman, E. Ben-Jacob, and D. J. Bergman, Thermopower of mesoscopic and disordered systems, *Phys. Rev. B* **51**, 17758 (1995).
- [100] M. Büttiker, Scattering theory of current and intensity noise correlations in conductors and wave guides, *Phys. Rev. B* **46**, 12485 (1992).
- [101] D. Sergi, Energy transport and fluctuations in small conductors, *Phys. Rev. B* **83**, 033401 (2011).
- [102] F. Zhan, S. Denisov, and P. Hänggi, Electronic heat transport across a molecular wire: Power spectrum of heat fluctuations, *Phys. Rev. B* **84**, 195117 (2011).
- [103] M. Büttiker, Coherent and sequential tunneling in series barriers, *IBM J. Res. Dev.* **32**, 63 (1988).
- [104] Y. Sumetskii and M. L. Fel'shtyn, Absolute transparency of an inelastic channel and the photovoltaic effect in the resonance tunneling through the two-well heterojunction, *Pis'ma Zh. Eksp. Teor. Fiz.* **53**, 24 (1991) [*JETP Lett.* **53**, 24 (1991)].
- [105] B. K. Agarwalla and D. Segal, Assessing the validity of the thermodynamic uncertainty relation in quantum systems, *Phys. Rev. B* **98**, 155438 (2018).
- [106] K. Prech, P. Johansson, E. Nyholm, G. T. Landi, C. Verdozzi, P. Samuelsson, and P. P. Potts, Entanglement and thermokinetic uncertainty relations in coherent mesoscopic transport, *Phys. Rev. Res.* **5**, 023155 (2023).
- [107] M. Büttiker, Y. Imry, and M. Y. Azbel, Quantum oscillations in one-dimensional normal-metal rings, *Phys. Rev. A* **30**, 1982 (1984).
- [108] M. Büttiker, Four-terminal phase-coherent conductance, *Phys. Rev. Lett.* **57**, 1761 (1986).
- [109] See Refs. [132,133] for related works discussing diffusive thermoelectricity in disordered nanowires.
- [110] R. Wang, C. Wang, J. Lu, and J.-H. Jiang, Inelastic thermoelectric transport and fluctuations in mesoscopic systems, *Adv. Phys.: X* **7**, 2082317 (2022).
- [111] J. B. Pendry, Quantum limits to the flow of information and entropy, *J. Phys. A: Math. Gen.* **16**, 2161 (1983).
- [112] R. S. Whitney, Finding the quantum thermoelectric with maximal efficiency and minimal entropy production at given power output, *Phys. Rev. B* **91**, 115425 (2015).
- [113] A. C. Barato and U. Seifert, Thermodynamic uncertainty relation for biomolecular processes, *Phys. Rev. Lett.* **114**, 158101 (2015).
- [114] K. Brandner, T. Hanazato, and K. Saito, Thermodynamic bounds on precision in ballistic multiterminal transport, *Phys. Rev. Lett.* **120**, 090601 (2018).
- [115] E. Potanina, C. Flindt, M. Moskalets, and K. Brandner, Thermodynamic bounds on coherent transport in periodically driven conductors, *Phys. Rev. X* **11**, 021013 (2021).
- [116] A. Dechant, Multidimensional thermodynamic uncertainty relations, *J. Phys. A: Math. Theor.* **52**, 035001 (2019).
- [117] M. Büttiker, Role of quantum coherence in series resistors, *Phys. Rev. B* **33**, 3020 (1986).
- [118] F. L. Curzon and B. Ahlborn, Efficiency of a Carnot engine at maximum power output, *Am. J. Phys.* **43**, 22 (1975).
- [119] D. Barker, S. Lehmann, L. Namazi, M. Nilsson, C. Thelander, K. A. Dick, and V. F. Maisi, Individually addressable double quantum dots formed with nanowire polytypes and identified by epitaxial markers, *Appl. Phys. Lett.* **114**, 183502 (2019).
- [120] C. Y. Chen, A. Shik, A. Pitanti, A. Tredicucci, D. Ercolani, L. Sorba, F. Beltram, and H. E. Ruda, Electron beam induced current in InSb-InAs nanowire type-III heterostructures, *Appl. Phys. Lett.* **101**, 063116 (2012).
- [121] P. Zolotavin, C. I. Evans, and D. Natelson, Substantial local variation of the Seebeck coefficient in gold nanowires, *Nanoscale* **9**, 9160 (2017).
- [122] V. I. Talyanskii, J. M. Shilton, M. Pepper, C. G. Smith, C. J. B. Ford, E. H. Linfield, D. A. Ritchie, and G. A. C. Jones, Single-electron transport in a one-dimensional channel by high-frequency surface acoustic waves, *Phys. Rev. B* **56**, 15180 (1997).
- [123] S. Hermelin, S. Takada, M. Yamamoto, S. Tarucha, A. D. Wieck, L. Saminadayar, C. Bäuerle, and T. Meunier, Electrons surfing on a sound wave as a platform for quantum optics with flying electrons, *Nature (London)* **477**, 435 (2011).
- [124] L. W. Molenkamp, H. van Houten, C. W. J. Beenakker, R. Eppenga, and C. T. Foxon, Quantum oscillations in the transverse voltage of a channel in the nonlinear transport regime, *Phys. Rev. Lett.* **65**, 1052 (1990).
- [125] S. K. Manikandan, E. Jussiau, and A. N. Jordan, Autonomous quantum absorption refrigerators, *Phys. Rev. B* **102**, 235427 (2020).
- [126] R. Puttock, C. Barton, E. Saugar, P. Klapetek, A. Fernández-Scarioni, P. Freitas, H. W. Schumacher, T. Ostler, O. Chubykalo-Fesenko, and O. Kazakova, Local thermoelectric response from a single Néel domain wall, *Sci. Adv.* **8**, eadc9798 (2022).
- [127] A. Cottet, W. Belzig, and C. Bruder, Positive cross-correlations due to dynamical channel blockade in a three-terminal quantum dot, *Phys. Rev. B* **70**, 115315 (2004).
- [128] J. P. Pekola and B. Karimi, Colloquium: Quantum heat transport in condensed matter systems, *Rev. Mod. Phys.* **93**, 041001 (2021).
- [129] D. Ryndyk, *Theory of Quantum Transport at Nanoscale* (Springer International Publishing, Cham, Switzerland, 2016).
- [130] W. G. van der Wiel, S. De Franceschi, J. M. Elzerman, T. Fujisawa, S. Tarucha, and L. P. Kouwenhoven, Electron transport through double quantum dots, *Rev. Mod. Phys.* **75**, 1 (2002).
- [131] D. S. Fisher and P. A. Lee, Relation between conductivity and transmission matrix, *Phys. Rev. B* **23**, 6851(R) (1981).
- [132] R. Bosisio, C. Gorini, G. Fleury, and J.-L. Pichard, Using activated transport in parallel nanowires for energy harvesting and hot-spot cooling, *Phys. Rev. Appl.* **3**, 054002 (2015).
- [133] K. A. Muttalib and S. Hershfield, Nonlinear thermoelectricity in disordered nanowires, *Phys. Rev. Appl.* **3**, 054003 (2015).